

Graphene-Tailored Thermodynamics and Kinetics to Fabricate Metal Borohydride Nanoparticles with High Purity and Enhanced Reversibility

Hongyu Zhang, Guanglin Xia,* Jian Zhang, Dalin Sun, Zaiping Guo, and Xuebin Yu*

Due to their ultrahigh theoretical capacity, metal borohydrides are considered to be one of the most promising candidate hydrogen storage materials. Their application still suffers, however, from high operating temperature, sluggish kinetics, and poor reversibility. Designing nanostructures is an effective way of addressing these issues, but seeking suitable approaches remains a big challenge. Here, a space-confined solid-gas reaction to synthesize $\text{Mg}(\text{BH}_4)_2$ nanoparticles supported on graphene is reported, which serves as the structural support for the dispersed $\text{Mg}(\text{BH}_4)_2$ nanoparticles. More notably, density functional theory calculations reveal that graphene could weaken both the $\text{Mg}-\text{H}$ bonds of MgH_2 and $\text{B}-\text{B}$ bonds of B_2H_6 , which could thermodynamically and kinetically facilitate the chemical transformation to synthesize $\text{Mg}(\text{BH}_4)_2$ with high purity. Because of the synergistic effects of both the significant reduction in particle size and the catalytic effect of graphene, an onset dehydrogenation temperature of $\approx 154^\circ\text{C}$ is observed for $\text{Mg}(\text{BH}_4)_2$ nanoparticles, and a complete dehydrogenation could be achieved at a temperature as low as 225°C , with the formation of MgB_2 as the by-product. This work provides a new perspective to tailoring the thermodynamics and kinetics of chemical reactions toward the favorable synthesis of functional inorganic materials.


1. Introduction

Hydrogen has great potential to become an ideal energy carrier in the future, due to its abundance, high energy density,

H. Y. Zhang, Prof. D. L. Sun, Prof. X. B. Yu
Department of Materials Science
Fudan University
Shanghai 200433, China
E-mail: yuxuebin@fudan.edu.cn

Dr. G. L. Xia, Prof. Z. P. Guo
Institute for Superconducting and Electronic Materials
University of Wollongong
North Wollongong, NSW 2522, Australia
E-mail: guanglin@uow.edu.au

Dr. J. Zhang
College of Automotive and Mechanical Engineering
Changsha University of Science and Technology
Changsha 410114, China
Prof. D. L. Sun, Prof. X. B. Yu
Shanghai Innovation Institute for Materials
Shanghai 200444, China

 The ORCID identification number(s) for the author(s) of this article can be found under <https://doi.org/10.1002/aenm.201702975>.

DOI: 10.1002/aenm.201702975

and environmental friendliness, but it requires a safe and efficient hydrogen storage technique for its extensive application.^[1,2] Storing hydrogen in a solid-state medium is considered to be the safest and most effective way to achieve the widespread application of hydrogen in the future.^[3–6] Owing to their high theoretical gravimetric and volumetric capacity for hydrogen, light metal borohydrides, such as LiBH_4 , $\text{Mg}(\text{BH}_4)_2$, and NaBH_4 , have great potential to be applied as practical hydrogen storage materials.^[6–9] Among them, $\text{Mg}(\text{BH}_4)_2$ possesses an attractive gravimetric capacity of 14.9 wt% and the highest volumetric capacity of 145–147 kg m^{-3} .^[10] More importantly, due to the much higher Pauling electronegativity (χ_p) of Mg ($\chi_p = 1.31$) compared to Ca, Li, and Na ($\chi_p = 1.00, 0.98, \text{ and } 0.93$, respectively), which leads to weaker ionic bonding strength and hence lower stability relative to these borohydrides, $\text{Mg}(\text{BH}_4)_2$ exhibits the

lowest temperature for hydrogen desorption among all the light metal borohydrides.^[11,12] The hydrogen storage process in $\text{Mg}(\text{BH}_4)_2$ could be generally described by the following Equation (1)^[13]



Based on the above equation, thermodynamic calculations reveal an enthalpy change of $-39 \text{ kJ mol}^{-1} \text{ H}_2$ for the dehydrogenation from $\text{Mg}(\text{BH}_4)_2$, enabling the hydrogen storage to occur within the temperature range of $20\text{--}75^\circ\text{C}$, which satisfies the practical requirements for proton exchange membrane fuel cells.^[14,15] Nevertheless, the operating temperature for the dehydrogenation from $\text{Mg}(\text{BH}_4)_2$ is generally over 300°C owing to its high kinetic barriers, which is mainly attributed to the sluggish diffusion of hydrogen and mass transport toward hydrogen desorption.^[16,17] Furthermore, the formation of stable intermediates generated from multistep reactions in the dehydrogenation significantly obstructs the reversibility of $\text{Mg}(\text{BH}_4)_2$; and hence, only negligible reversibility is observed from its dehydrogenated products, even under harsh conditions, including high hydrogen pressure and high temperature (e.g., 90 MPa, 400°C),^[18] which is regarded as one of the major

obstacles for the practical application of $\text{Mg}(\text{BH}_4)_2$ for on-board hydrogen storage systems.

To date, the main strategies to improve the hydrogen storage performance of $\text{Mg}(\text{BH}_4)_2$ involve the addition of catalysts and reduction of the particle size of $\text{Mg}(\text{BH}_4)_2$. Although the adoption of catalysts could indeed modify the kinetics of $\text{Mg}(\text{BH}_4)_2$ to some extent, the improvement is very much limited by the density of active sites and the selectivity, accessibility, and stability of the catalyst, as well as the sluggish mass transport and the formation of stable intermediates arising from the dehydrogenation process.^[19–24] On the other hand, reduction of the particle size down to nanometer range could directly reduce the barrier of reaction pathways for both hydrogen diffusion and mass transport in the solid state, which would play an important role in relieving the kinetic constraints, and hence, could effectively enhance the dehydrogenation and hydrogenation kinetics.^[25–27] In addition, nanostructuring of metal borohydrides could generate large specific surface area, grain boundaries, defects, and increased concentrations of steps, kinks, and corner atoms, which could thermodynamically destabilize the borohydrides toward enhanced hydrogen storage performance.^[28,29]

Confining or anchoring active materials inside porous hosts is an effective way to synthesize $\text{Mg}(\text{BH}_4)_2$ nanoparticles (NPs) by virtue of the structural support of scaffolds.^[30–32] Solution impregnation and solid-gas reactions between nanoconfined MgH_2 NPs and diborane (B_2H_6), according to the Equation (2), are common strategies to incorporate $\text{Mg}(\text{BH}_4)_2$ into porous support materials.^[33–37] Nevertheless, some unresolved issues significantly hinder the utilization of these strategies to fabricate nanostructured $\text{Mg}(\text{BH}_4)_2$ with high density and purity. In terms of the solution impregnation method, the tedious infiltration process and the tremendous decrease in systematic storage capacity due to the introduction of a large amount of inactive scaffolds for hydrogen storage (more than 55 wt% in general) significantly limits its practical application.^[36,38] In addition, irregular spatial distribution and the agglomeration of $\text{Mg}(\text{BH}_4)_2$ NPs are usually observed due to the lack of control over the infiltration process, which would significantly attenuate the effects of space confinement toward improving the performance of $\text{Mg}(\text{BH}_4)_2$.^[37] More importantly, the favorable adsorption of $\text{Mg}(\text{BH}_4)_2$ from its solvent would not only significantly reduce the purity of the resultant $\text{Mg}(\text{BH}_4)_2$ NPs, but also contaminate the released hydrogen upon thermal treatment.^[37] Alternatively, although the synthesis of $\text{Mg}(\text{BH}_4)_2$ NPs through the solid-gas reaction between B_2H_6 and the nanoconfined MgH_2 NPs suffers from almost the same drawbacks as the nanoconfinement of $\text{Mg}(\text{BH}_4)_2$ via solution infiltration caused by the nanoconfinement of MgH_2 NPs, the presence of organic solvent would be avoided owing to its relatively weak interaction with MgH_2 . The simultaneous formation of $\text{MgB}_{12}\text{H}_{12}$ with high thermodynamic stability during the solid-gas reaction, however, significantly decreases the purity of the as-synthesized $\text{Mg}(\text{BH}_4)_2$ NPs and the releasable capacity of the whole system.^[27,28] Therefore, developing a new chemical synthesis strategy to fabricate homogeneous $\text{Mg}(\text{BH}_4)_2$ NPs with both high purity and high density is still a big challenge, but it is of particular importance for further improvement of the hydrogen storage performance of $\text{Mg}(\text{BH}_4)_2$ toward practical applications



To address all the above issues, we present a graphene-tailored solid-gas reaction strategy to fabricate uniform $\text{Mg}(\text{BH}_4)_2$ NPs homogeneously distributed on graphene, which plays a vital role in thermodynamically and kinetically enhancing the chemical reaction between MgH_2 NPs and B_2H_6 to synthesize borohydrides. Specifically, graphene-supported homogeneous MgH_2 NPs (denoted as MH-Gr) with an average particle size of ≈ 8 nm were synthesized through a bottom-up self-assembly strategy as in “smart” nanoreactors (**Figure 1**). Subsequently, a space-confined solid-gas reaction between B_2H_6 and graphene-supported MgH_2 NPs under the protection of hydrogen was developed to realize the synthesis of $\text{Mg}(\text{BH}_4)_2$ NPs that are uniformly anchored on graphene (denoted as MBH-Gr) with high loading amount and purity. First, the reduction of the particle size of MgH_2 NPs down to ≈ 8 nm significantly decreases the mass transport distance for the solid-gas reaction, which could kinetically promote the formation of $\text{Mg}(\text{BH}_4)_2$ from MgH_2 . More importantly, density functional theory (DFT) calculations demonstrate that the presence of graphene could not only weaken the B–B bonds of B_2H_6 and the Mg–H bonds of MgH_2 , but also stabilize the formation of $\text{Mg}(\text{BH}_4)_2$, so that it therefore thermodynamically enhances the solid-gas reaction to synthesize $\text{Mg}(\text{BH}_4)_2$ NPs. In addition, the nanoreactor composed of MgH_2 NPs and graphene exhibits porous and large interspace structure, which provides facile pathways for the transport of B_2H_6 and facilitates sufficient and uniform contact between MgH_2 NPs and B_2H_6 , promoting the formation of $\text{Mg}(\text{BH}_4)_2$ NPs. Moreover, the uniform distribution of MgH_2 on graphene with a large interparticle distance through the bottom-up self-assembly approach could guide the formation of homogeneous $\text{Mg}(\text{BH}_4)_2$ NPs with high loading, which results in high hydrogen storage capacity and energy density of the whole system. As a result, the as-synthesized MBH-Gr exhibits unique structural and hydrogen storage properties, including stable structural integrity, fast hydrogen desorption, low activation barriers, and remarkable reversible hydrogen storage performance.

2. Results and Discussion

Graphene-supported homogeneous MgH_2 NPs were first synthesized through the hydrogenation-induced solvothermal reaction of dibutyl magnesium.^[39] Owing to the favorable adsorption of both dibutyl magnesium and MgH_2 on graphene, large amounts of MgH_2 NPs are observed to be uniformly dispersed on graphene with a rippled paper-like morphology (**Figure 2a**), with an absence of unattached nanoparticles. The cross-sectional scanning electron microscope (SEM) image reveals the layer-by-layer stacking of graphene, leading to the formation of porous structure with massive out-of-plane macropores (**Figure 2b**). The uniform distribution of MgH_2 NPs (**Figure 2c**), which exhibit an average size of 8 nm (**Figure S1**, Supporting Information), was further verified by transmission electron microscopy (TEM). The high-resolution TEM (HRTEM) image of MH-Gr in the inset of **Figure 2c** clearly shows a d -spacing of 1.595 Å, corresponding to the (220) planes

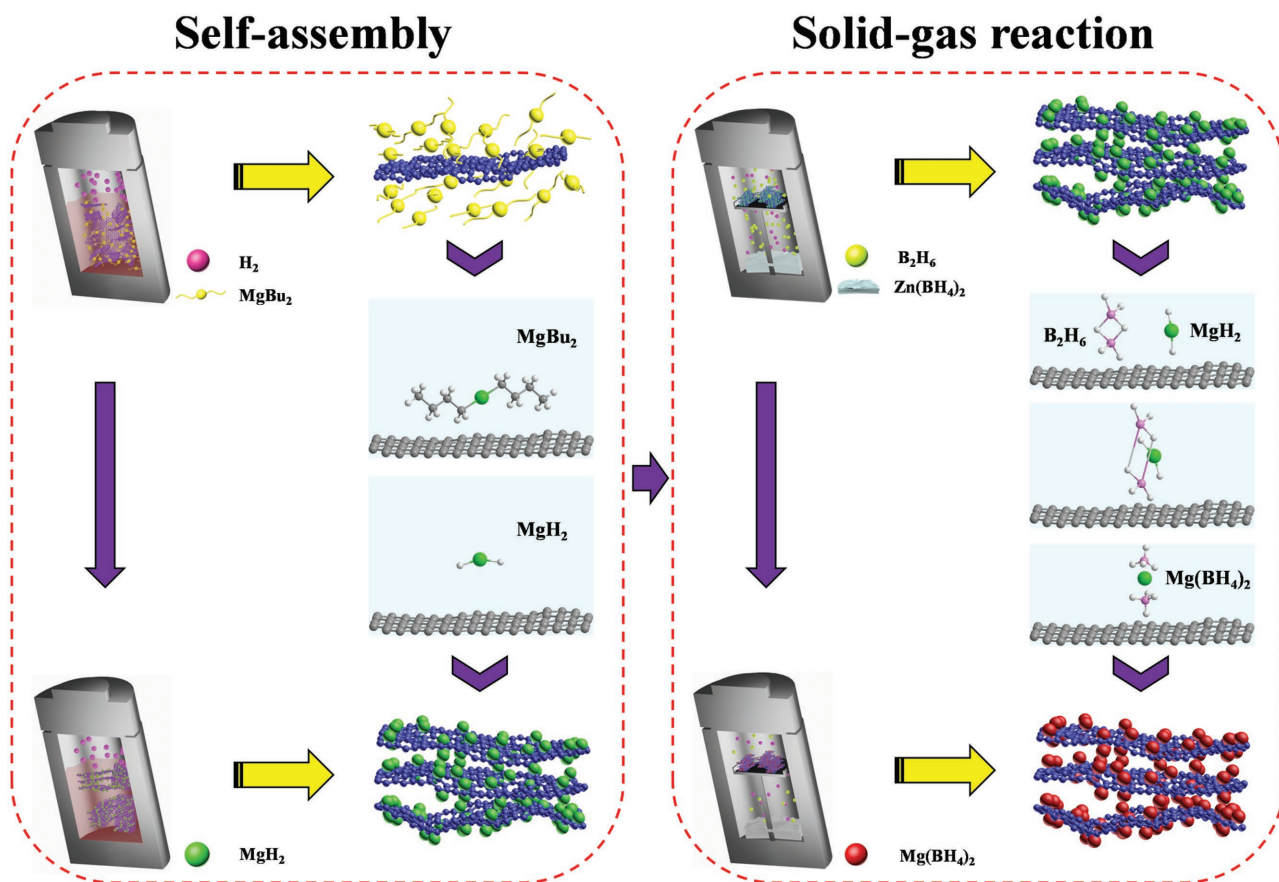


Figure 1. Schematic illustration of the fabrication of MBH-Gr via space-confined solid-gas reaction, a) Self-assembly of MgH_2 NPs on graphene (MH-Gr) via a bottom-up solvothermal reaction, serving as the “smart” nanoreactor, b) the graphene-tailored solid-gas reaction between MH-Gr and B_2H_6 to synthesize $\text{Mg}(\text{BH}_4)_2$ NPs that are uniformly distributed on graphene (MBH-Gr) under the protection of hydrogen.

of MgH_2 , which demonstrates the formation of $\beta\text{-MgH}_2$ and coincides well with the X-ray diffraction (XRD) results (Figure 3a). Moreover, the scanning TEM (STEM) image (Figure 2g) clearly illustrates the homogeneous dispersion of MgH_2 NPs with a large interparticle distance between the individual NPs. The corresponding element mapping further demonstrates the uniform distribution of C and Mg elements (Figure S2, Supporting Information). The large interparticle space on the flexible graphene layers could effectively alleviate aggregation and particle growth during the solid-gas reaction to form $\text{Mg}(\text{BH}_4)_2$, and meanwhile, the porous structure of graphene could provide facile pathways for the transportation of B_2H_6 to react with each MgH_2 NP.

Subsequently, MH-Gr was then adopted as the “smart” nanoreactor to synthesize $\text{Mg}(\text{BH}_4)_2$ NPs via the space-confined solid-gas reaction between the MgH_2 NPs and B_2H_6 on graphene. The XRD patterns (Figure 3a) exhibit the characteristic peaks belonging to $\text{Mg}(\text{BH}_4)_2$, along with the disappearance of MgH_2 , which demonstrates the successful synthesis of $\text{Mg}(\text{BH}_4)_2$ based on the solid-gas reaction between B_2H_6 and graphene-supported MgH_2 NPs. It should be noted that, although the Fourier-transform infrared (FTIR) spectra further confirm the synthesis of $\text{Mg}(\text{BH}_4)_2$ by the presence of its characteristic peaks, a weak peak at 2478 cm^{-1} is also observed, indicating the simultaneous formation of $\text{MgB}_{12}\text{H}_{12}$.^[40] By

comparison, without the presence of graphene, MgH_2 could be still observed without the formation of crystalline $\text{Mg}(\text{BH}_4)_2$ under the same conditions, based on the reaction between MgH_2 NPs and B_2H_6 , and meanwhile, a strong peak belonging to $\text{MgB}_{12}\text{H}_{12}$ could be observed in the FTIR spectra (Figure S3, Supporting Information), which coincides well with the previous reports.^[35,36] This directly confirms the important role of graphene in thermodynamically and kinetically facilitating the generation of $\text{Mg}(\text{BH}_4)_2$. In order to elucidate the mechanism underlying the formation of $\text{MgB}_{12}\text{H}_{12}$, first-principles calculations were performed based on the DFT. They reveal that the enthalpy for the reaction between MgH_2 and B_2H_6 to form $\text{Mg}(\text{BH}_4)_2$ is around -240 kJ mol^{-1} , while the value for the formation of $\text{MgB}_{12}\text{H}_{12}$ reaches -295 kJ mol^{-1} , which validates the formation of $\text{MgB}_{12}\text{H}_{12}$ from the reaction between MgH_2 and B_2H_6 through thermal heating, which is energetically favorable compared with the synthesis of $\text{Mg}(\text{BH}_4)_2$ (Figure S4, Supporting Information). In strong contrast, with the support of graphene, the enthalpy for the formation of $\text{Mg}(\text{BH}_4)_2$ decreases to -308 kJ mol^{-1} , approaching that of $\text{MgB}_{12}\text{H}_{12}$ (-320 kJ mol^{-1}) under the same conditions, demonstrating that the presence of graphene could thermodynamically facilitate the synthesis of $\text{Mg}(\text{BH}_4)_2$. The optimized geometry illustrates that the lengths of the Mg–H bonds of MgH_2 and the B–B bonds of B_2H_6 are increased to 1.717 and 1.757 Å, respectively, while the B–B

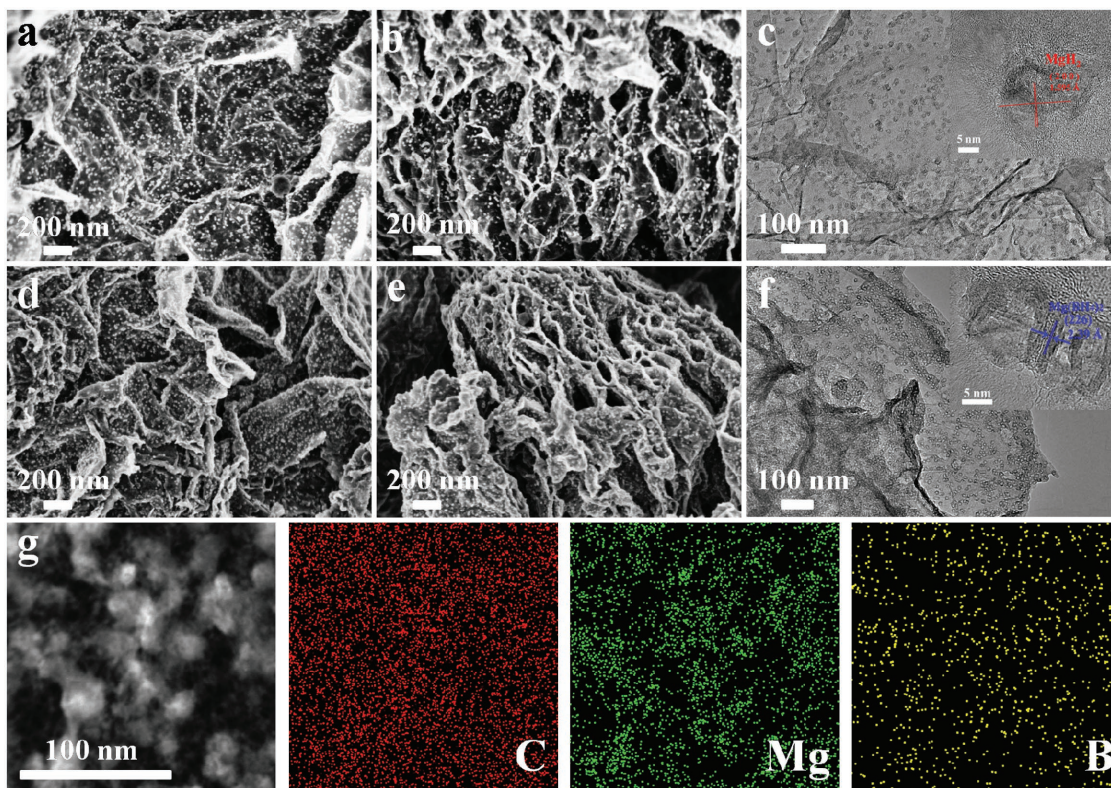


Figure 2. a) SEM, b) cross-sectional SEM, and c) TEM images of MH-Gr. d) SEM, e) cross-sectional SEM, and f) TEM images of MBH-Gr. g) Representative STEM image and the corresponding elemental mapping of MBH-Gr. The insets of (c, f) exhibit the corresponding HRTEM images of MH-Gr and MBH-Gr, respectively.

distance of $\text{Mg}(\text{BH}_4)_2$ is decreased to 4.109 \AA with the support of graphene (Figures 3e, f). This therefore confirms that graphene could weaken both the Mg–H and B–B bonds and stabilize the formation of $\text{Mg}(\text{BH}_4)_2$, which directly demonstrates that graphene could thermodynamically promote the solid-gas reaction between MgH_2 and B_2H_6 to synthesize $\text{Mg}(\text{BH}_4)_2$.

To fully depress the reaction to form $\text{MgB}_{12}\text{H}_{12}$ and promote the formation of $\text{Mg}(\text{BH}_4)_2$, the hydrogen pressure was increased from around 10 to 50 atm. It could be clearly observed that, with the increase in the hydrogen pressure, the peak at 2478 cm^{-1} indexed to $\text{MgB}_{12}\text{H}_{12}$ weakens, indicating that the formation of $\text{MgB}_{12}\text{H}_{12}$ is depressed (Figure 3b). Upon increasing the hydrogen pressure to 50 atm, all the peaks present could be assigned to the characteristic peaks of $\text{Mg}(\text{BH}_4)_2$ with the complete disappearance of $\text{MgB}_{12}\text{H}_{12}$, which confirms the formation of $\text{Mg}(\text{BH}_4)_2$ with high purity (Figure 3b). SEM and TEM images (Figure 2d–f) clearly illustrate the presence of uniform nanoparticles homogeneously distributed on graphene without obvious aggregation, validating the well-preserved nature of the morphology after the solid-gas reaction. This indicates that flexible graphene could effectively prevent the agglomeration of $\text{Mg}(\text{BH}_4)_2$ NPs during thermal treatment. The HRTEM image exhibits some lattice fringes with interplanar spacing of 2.4 \AA (inset of Figure 2f), corresponding to the (226) planes of $\text{Mg}(\text{BH}_4)_2$, which agrees well with the XRD results (Figure 3a) and further demonstrates the synthesis of $\text{Mg}(\text{BH}_4)_2$. Furthermore, the elemental mappings of Mg, B, and C coincide well with each other for the as-synthesized MBH-Gr

(Figure 2g), which provides further evidence for the uniform anchoring of the $\text{Mg}(\text{BH}_4)_2$ NPs on graphene. It is noteworthy that the average particle size of the $\text{Mg}(\text{BH}_4)_2$ NPs on graphene increases slightly to 10 nm due to the incorporation of the foreign element (B) into the MgH_2 NPs (Figure S1b, Supporting Information), indirectly corroborating the thorough conversion from MgH_2 NPs to $\text{Mg}(\text{BH}_4)_2$ NPs. The intimate and uniform contact between both the MgH_2 NPs and the $\text{Mg}(\text{BH}_4)_2$ NPs and the graphene induced by the self-assembly strategy could strengthen the effects of graphene toward tailoring their bonding structures, which could thermodynamically and kinetically improve this chemical transformation. More importantly, the homogeneous distribution of the resultant $\text{Mg}(\text{BH}_4)_2$ NPs with a uniform particle size of 10 nm could significantly shorten the diffusion pathways of hydrogen and hence, improve the H-exchange kinetics of hydrogen desorption and absorption, while graphene could effectively prevent the agglomeration and particle growth of $\text{Mg}(\text{BH}_4)_2$ NPs during the hydrogen storage process, which endows the as-synthesized $\text{Mg}(\text{BH}_4)_2$ NPs with great potential to achieve advanced hydrogen storage performance.

Figure 4a shows the mass spectroscopy (MS) results for the hydrogen desorption from graphene-supported $\text{Mg}(\text{BH}_4)_2$ NPs in comparison with the ball-milled $\text{Mg}(\text{BH}_4)_2$ (BM- $\text{Mg}(\text{BH}_4)_2$) and a composite of ball-milled $\text{Mg}(\text{BH}_4)_2$ and graphene (BM-MBH-Gr). The hydrogen desorption of pure $\text{Mg}(\text{BH}_4)_2$ starts at $\approx 296 \text{ }^\circ\text{C}$, with two dehydrogenation peaks at ≈ 336 and $\approx 390 \text{ }^\circ\text{C}$, which agrees well with the thermogravimetric (TG)

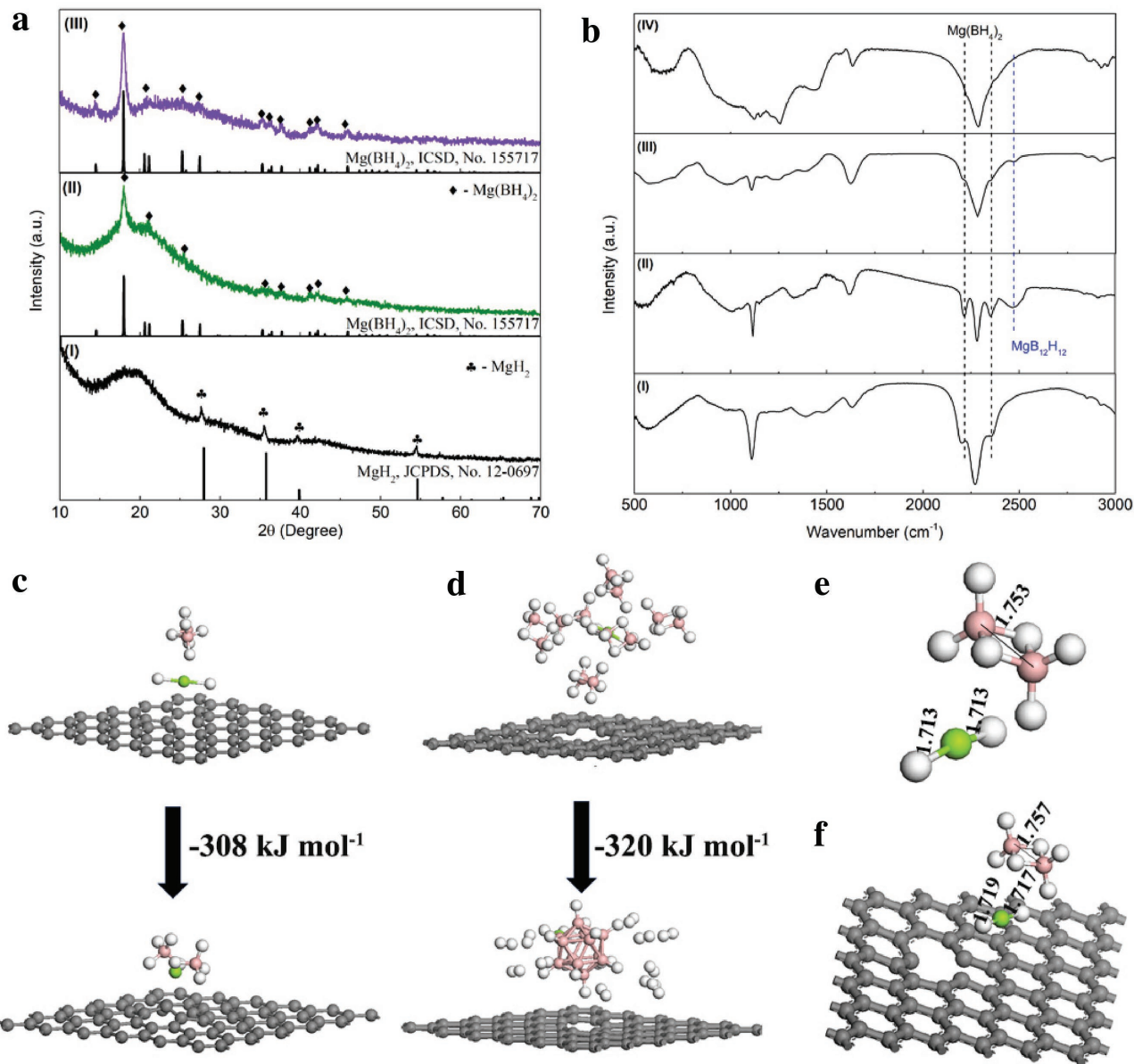


Figure 3. a) XRD patterns of I) MH-Gr and MBH-Gr synthesized under hydrogen pressure of II) 10 atm and III) 50 atm, respectively. b) FTIR spectra of MBH-Gr synthesized under hydrogen pressure of II) 10 atm, III) 20 atm, and IV) 50 atm, respectively, including pure Mg(BH₄)₂ I) for comparison. Relaxed atomic configurations of MgH₂ and B₂H₆, and calculated reaction enthalpies for the formation of c) Mg(BH₄)₂ and d) MgB₁₂H₁₂ from the reaction between MgH₂ and B₂H₆ with the support of graphene. Relaxed atomic configurations of MgH₂ and B₂H₆ e) without and f) with the support of graphene. Gray, white, green, and pink spheres are C, H, Mg, and B atoms, respectively.

results and is analogous to what was previously reported.^[41] A total dehydrogenation capacity of ≈ 12.85 wt% was observed for pure Mg(BH₄)₂, which is slightly lower than the theoretical gravimetric capacity of Mg(BH₄)₂ (≈ 14.9 wt%), indicating its incomplete decomposition. This is verified by the XRD patterns (Figure S5, Supporting Information) and FTIR spectra (Figure S6, Supporting Information), which demonstrate that the dehydrogenation products of pure Mg(BH₄)₂ at 450 °C are mainly composed of Mg, MgB₁₂H₁₂, and amorphous boron, with the absence of MgB₂, in good agreement with the literature.^[11] The formation of MgB₁₂H₁₂ and amorphous boron instead of MgB₂ would not only decrease the releasable capacity of Mg(BH₄)₂,

but also significantly limit the reversibility of the dehydrogenated products due to their high thermodynamic stability.^[42] Upon the introduction of graphene into Mg(BH₄)₂, the onset temperature for the dehydrogenation of the BM-MBH-Gr is decreased to ≈ 257 °C, with a peak temperature at ≈ 299 °C, which represents a slight reduction compared with pure Mg(BH₄)₂. It indicates that the presence of graphene could play a catalytic role in the hydrogen desorption process of Mg(BH₄)₂. Unfortunately, similar dehydrogenation products were observed for BM-MBH-Gr as compared with pure Mg(BH₄)₂ (Figures S7 and S8, Supporting Information), indicating that the reaction pathways for the dehydrogenation from Mg(BH₄)₂ are unchanged

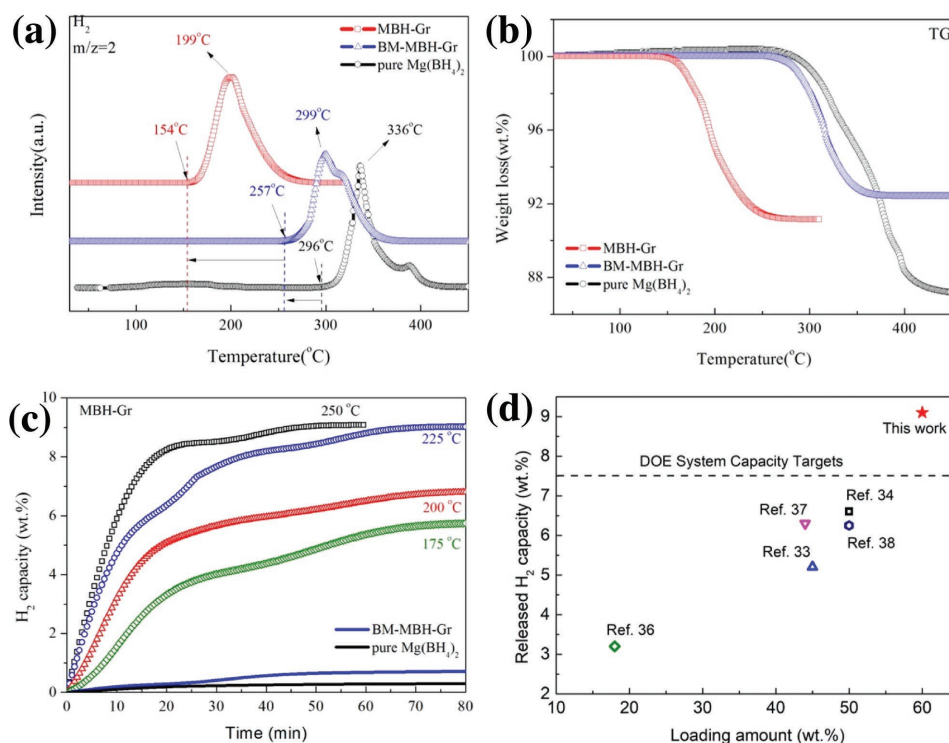


Figure 4. a) Mass spectra and b) thermogravimetric analysis curves of the as-synthesized MBH-Gr compared with BM-MBH-Gr and pure Mg(BH₄)₂. c) Isothermal dehydrogenation of the as-synthesized MBH-Gr at various temperatures, with BM-MBH-Gr and pure Mg(BH₄)₂ at 175 °C included for comparison. d) Systematic comparison of the loading amount and the highest hydrogen capacity that could be released below 250 °C of MBH-Gr and nanoconfined Mg(BH₄)₂ NPs in the hosts reported in the previous literature (Table S1, Supporting Information) with our results in the present work.

after the mechanical milling with graphene. In strong contrast, the as-synthesized MBH-Gr exhibits a one-step decomposition, with the onset and peak temperature downshifted to 154 and 199 °C, 103 and 100 °C lower than that of the ball-milled composite of Mg(BH₄)₂ and graphene, respectively. The hydrogen desorption of MBH-Gr mainly occurs in the temperature range from 154 to 260 °C, while the dehydrogenation of MBH-Gr is mainly derived from the decomposition in the temperature region from 200 to 280 °C, with a peak temperature at 242 °C (Figure S9, Supporting Information), indirectly confirming the uniform formation of Mg(BH₄)₂ NPs from the solid-gas reaction between graphene-supported MgH₂ NPs and B₂H₆, and the absence of MgH₂. Furthermore, it is interesting to note that the hydrogen desorption of MBH-Gr is almost complete before the start of the dehydrogenation process for both BM-MBH-Gr and pure Mg(BH₄)₂, which further verifies the significantly enhanced dehydrogenation performance that is attributable to the synergistic effects of both the significant reduction of particle size down to ≈10 nm and the catalytic role of graphene. The complete dehydrogenation of MBH-Gr below 300 °C could be confirmed by the XRD and FTIR results on the dehydrogenated products, in which only diffraction peaks of MgB₂ are present, with the disappearance of Mg(BH₄)₂ (Figures S10 and S11, Supporting Information), while the presence of Mg(BH₄)₂ could be clearly observed for both BM-MBH-Gr and pure Mg(BH₄)₂ under the same conditions (Figures S5–S8, Supporting Information), which agrees well with the MS results. This provides further evidence of the much superior hydrogen

storage performance of MBH-Gr compared with pure Mg(BH₄)₂ and the ball-milled composite of Mg(BH₄)₂ and graphene. More importantly, no characteristic peaks assigned to B–H bonds were detected for MBH-Gr after the dehydrogenation process, indicating the absence of MgB₁₂H₁₂. It is widely demonstrated that bulk Mg(BH₄)₂ decomposes through a polymerization process with the formation of MgB₁₂H₁₂ as the main intermediate products^[14,43,44] and, with the increase of reaction temperature, all B-containing species could be transformed into MgB₂.^[40] In the terms of MBH-Gr, the tremendous decrease of particle size of Mg(BH₄)₂ could effectively reduce the distance for the diffusion of Mg, B, and H in the compound and facilitate the mass transport, which lowers the kinetic barrier of the reaction to form MgB₂ with favorable thermodynamics, thus promoting the direct formation of MgB₂. These results highlight the important roles of nanostructuring and graphene in optimizing the reaction pathways and hence improving both the thermodynamics and the kinetics of Mg(BH₄)₂ toward advanced hydrogen storage performance.

A hydrogen capacity of ≈8.96 wt% could be achieved for MBH-Gr (Figure 4b), which corresponds to a mass loading of ≈60% for Mg(BH₄)₂ NPs distributed on graphene, considering the complete dehydrogenation of Mg(BH₄)₂ to form MgB₂. Such a high loading is much superior to those in the reported results (Table S1, Supporting Information), which ensures high systematic energy density and satisfies the requirement for practical applications (Figure 4d). The isothermal dehydrogenation kinetics of MBH-Gr was further investigated in comparison

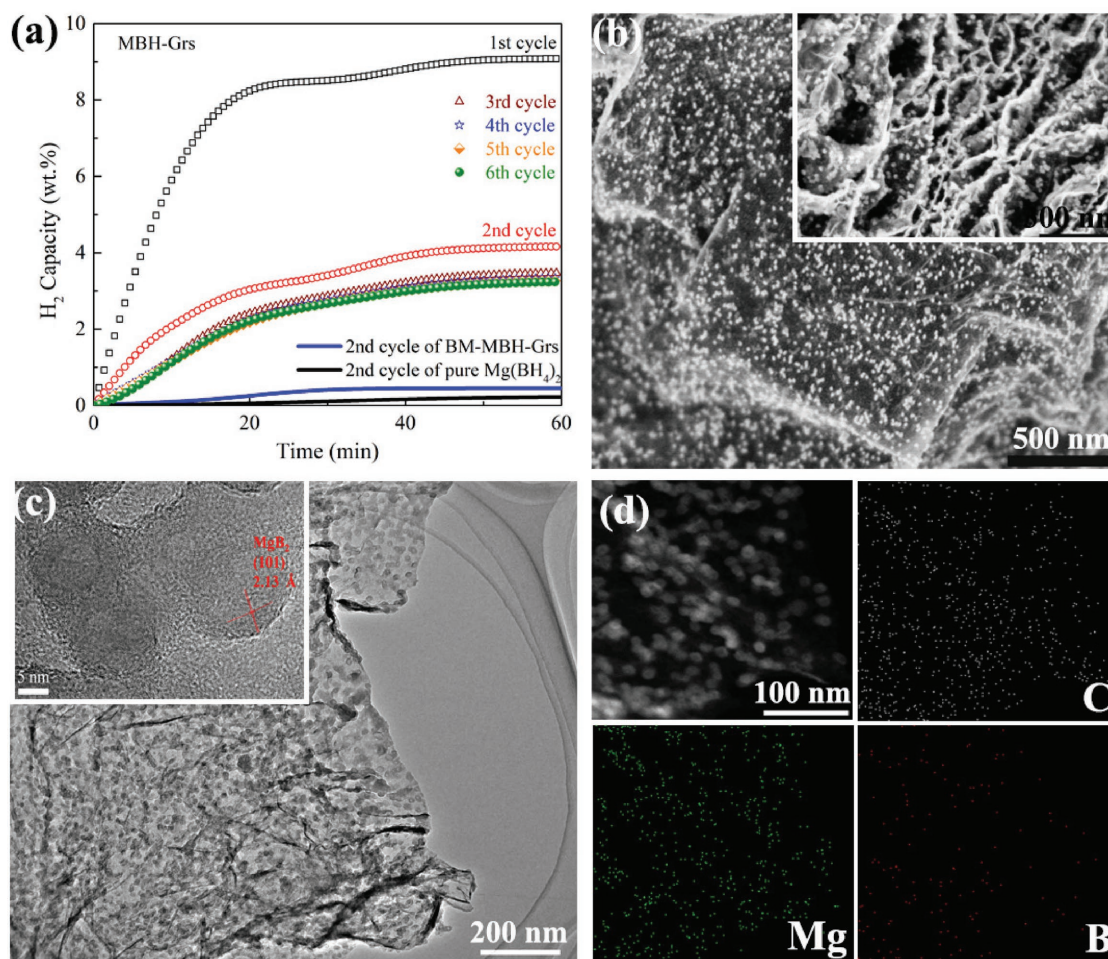


Figure 5. a) Reversible-dehydrogenation hydrogen storage capacities of MBH-Gr, with BM-MBH-Gr and pure $\text{Mg}(\text{BH}_4)_2$ at 250°C included for comparison. b) SEM and c) TEM images, and d) representative STEM image and the corresponding elemental mapping of the as-synthesized MBH-Gr after three cycles of dehydrogenation and rehydrogenation. The insets of (b,c) exhibit the corresponding cross-sectional SEM and HRTEM images of MH-Gr and MBH-Gr, respectively.

with the mechanically milled $\text{Mg}(\text{BH}_4)_2$ and the composite of $\text{Mg}(\text{BH}_4)_2$ and graphene (Figure 4c). Only a negligible amount of hydrogen could be released from either the pure $\text{Mg}(\text{BH}_4)_2$ or the BM-MBH-Gr within 80 min at 175°C . In strong contrast, the capacity released from MBH-Gr could approach 5.73 wt% under identical conditions. As expected, with an increase in temperature from 175 to 225°C , the capacity released from MBH-Gr increases. In particular, a hydrogen capacity of ≈ 9.04 wt% could be rapidly released in a 50 min period at a temperature as low as 250°C , which far exceeds the US Department of Energy hydrogen storage target in 2017 and the values reported in previous related works (Figure 4d). In order to quantitatively evaluate the significantly enhanced hydrogen desorption kinetics of MBH-Gr, the apparent activation energy (E_a) for the dehydrogenation from MBH-Gr was determined by combining the Johanson–Mehl–Avrami–Kolmogorov results (Equation S1, Supporting Information) with the Arrhenius equation (Equation S2, Supporting Information) according to the isothermal hydrogen desorption curves at various temperatures. The E_a value for the desorption of MBH-Gr is calculated to be 28.96 kJ mol^{-1} (Figure S12, Supporting

Information), much lower than that for pure $\text{Mg}(\text{BH}_4)_2$ (45.9 kJ mol^{-1}).^[38] This provides direct proof of the significant improvement of the hydrogen desorption kinetics for graphene-supported $\text{Mg}(\text{BH}_4)_2$ NPs, originating mostly from the shortened distances for mass transport, owing to the tremendous size reduction, and the enhanced catalytic effects due to the homogeneous distribution of $\text{Mg}(\text{BH}_4)_2$ NPs on graphene with intimate contact.

The cycling performance of graphene-supported $\text{Mg}(\text{BH}_4)_2$ NPs, which is a critically challenging aspect for their practical application, was further investigated by isothermal hydrogenation and dehydrogenation at 250°C using the volumetric method, as compared with the ball-milled composite of $\text{Mg}(\text{BH}_4)_2$ and graphene (Figure 5a). It is demonstrated that only a negligible amount of hydrogen is released from either pure $\text{Mg}(\text{BH}_4)_2$ or the BM-MBH-Gr after one cycle of hydrogenation at 250°C , indicating their poor reversibility, which should be attributed to the formation of amorphous boron and $\text{MgB}_{12}\text{H}_{12}$ with high thermodynamic stability. By comparison, the hydrogen capacity released from MBH-Gr under the same conditions still reaches 4.13 and 3.47 wt%

in the second and third cycles, respectively, suggesting the favorable reversibility of graphene-supported $\text{Mg}(\text{BH}_4)_2$ NPs. XRD patterns of MBH-Gr after two cycles of hydrogenation exhibit much weaker peaks of MgB_2 compared with the dehydrogenated products (Figure S10, Supporting Information), which implies the partial transformation of MgB_2 into amorphous species. Based on the FTIR spectra of MBH-Gr after two cycles of hydrogenation, the characteristic peaks indexed to B–H bonds of $\text{Mg}(\text{BH}_4)_2$ could be clearly observed, with a weak peak belonging to $\text{MgB}_{12}\text{H}_{12}$ (Figure S11, Supporting Information). These results demonstrate that the MgB_2 was partially converted to amorphous $\text{Mg}(\text{BH}_4)_2$ with the formation of a small amount of $\text{MgB}_{12}\text{H}_{12}$, which indicates the successful reversibility of $\text{Mg}(\text{BH}_4)_2$ with the support of graphene. The TEM and SEM images (Figures 5b,c) demonstrate that the structure of MBH-Gr is well preserved after three cycles of hydrogen storage, and no obvious agglomeration is observed, demonstrating the superior physical stability owing to the intimate contact between $\text{Mg}(\text{BH}_4)_2$ NPs and graphene, which contributes to the favorable reversibility of the as-synthesized MBH-Gr to some extent. After three cycles of dehydrogenation for MBH-Gr, the formation of MgB_2 could be further verified by the HRTEM image (inset of Figure 5c), which exhibits an interplanar spacing of 0.21 nm, corresponding to the (101) planes of hexagonal MgB_2 . The corresponding elemental mapping of Mg, B, and C (Figure 5d) further demonstrates the uniform distribution of $\text{Mg}(\text{BH}_4)_2$ NPs in the composite after thermal cycling for dehydrogenation and hydrogenation. The average particle size of MgB_2 is calculated to be ≈ 10.3 nm (Figure S13, Supporting Information), which effectively shortens the diffusion pathways for hydrogen and mass transport with enhanced interfacial reactivity, thus leading to the favorable reaction between MgB_2 and hydrogen to regenerate $\text{Mg}(\text{BH}_4)_2$. It is interesting to note that, due to this unique structure and the favorable formation of MgB_2 , a reversible hydrogen capacity of 3.24 wt% could still be achieved for MBH-Gr in the 6th cycle, and the kinetics of dehydrogenation is well maintained from the 3rd to 6th cycle. The cycling stability and reversible capacity are advanced compared to some other reported works under the same or more severe conditions (Table S2, Supporting Information).^[22,23,45] It provides further evidence to the superior cycling stability of graphene-supported $\text{Mg}(\text{BH}_4)_2$ NPs.

3. Conclusion

In summary, we have developed a graphene-confined solid-gas reaction to fabricate $\text{Mg}(\text{BH}_4)_2$ NPs with high purity that are homogeneously anchored on graphene, by virtue of graphene-supported MgH_2 NPs functioning as smart nanoreactors. Detailed DFT calculations reveal that the presence of graphene could thermodynamically promote the formation of $\text{Mg}(\text{BH}_4)_2$ NPs via weakening the Mg–H bonds of MgH_2 and the B–B bonds of B_2H_6 , and stabilizing $\text{Mg}(\text{BH}_4)_2$, while the reduction of particle size of MgH_2 to ≈ 8 nm and the porous structure could significantly improve the reaction kinetics due to the shortened diffusion pathways for mass transport and the facile transport of B_2H_6 to react with individual MgH_2 NPs. In addition, the homogeneous distribution of MgH_2

NPs on the flexible graphene with intimate contact could effectively avoid the growth and aggregation of nanoparticles during chemical transformation, leading to the formation of homogeneous $\text{Mg}(\text{BH}_4)_2$ NPs with an average particle size of ≈ 10 nm anchored on graphene. Due to this unique structure, graphene-supported $\text{Mg}(\text{BH}_4)_2$ NPs exhibited an onset dehydrogenation temperature of 154 °C and a hydrogen capacity of ≈ 9.04 wt% at a temperature as low as 225 °C. More importantly, owing to the favorable formation of MgB_2 and the reduction of particle size to ≈ 10.3 nm, a reversible systematic capacity of 4.13 wt% was achieved at 300 °C. This novel strategy provides new insights to improve both the thermodynamics and the kinetics of the chemical reactions to synthesize metal borohydrides for advanced hydrogen storage performance. Moreover, the unique mechanism for the synthesis of metal borohydrides could animate further studies on the mechanisms of interface-enhanced chemical reactions.

Supporting Information

Supporting Information is available from the Wiley Online Library or from the author.

Acknowledgements

This work was partially supported by the National Science Fund for Distinguished Young Scholars (51625102), National Key Research and Development Program of China (2017YFA0204600), the National Natural Science Foundation of China (51471053), the Science and Technology Commission of Shanghai Municipality (17XD1400700), and a Discovery Early Career Researcher Award (DE170100362). The authors also would like to thank Prof. Dianwu Zhou in Hunan University for the support of the DFT calculations software and Dr. Tania Silver for critical reading of the manuscript.

Conflict of Interest

The authors declare no conflict of interest.

Keywords

borohydrides, graphene, hydrogen storage, kinetics, magnesium hydride

Received: October 26, 2017
Revised: November 17, 2017
Published online: January 15, 2018

- [1] L. Schlapbach, A. Züttel, *Nature* **2001**, 414, 353.
- [2] M. B. Ley, L. H. Jepsen, Y.-S. Lee, Y. W. Cho, J. M. Bellosta von Colbe, M. Dornheim, M. Rokni, J. O. Jensen, M. Sloth, Y. Filinchuk, J. E. Jørgensen, F. Besenbacher, T. R. Jensen, *Mater. Today* **2014**, 17, 122.
- [3] Y. Liu, Y. Yang, M. Gao, H. Pan, *Chem. Rec.* **2016**, 16, 189.
- [4] M. Paskevicius, L. H. Jepsen, P. Schouwink, R. Cerny, D. B. Ravnsbaek, Y. Filinchuk, M. Dornheim, F. Besenbacher, T. R. Jensen, *Chem. Soc. Rev.* **2017**, 46, 1565.

- [5] R. Mohtadi, S.-I. Orimo, *Nat. Rev. Mater.* **2016**, *2*, 16091.
- [6] Q. Lai, M. Paskevicius, D. A. Sheppard, C. E. Buckley, A. W. Thornton, M. R. Hill, Q. Gu, J. Mao, Z. Huang, H. K. Liu, Z. Guo, A. Banerjee, S. Chakraborty, R. Ahuja, K.-F. Aguey-Zinsou, *ChemSusChem* **2015**, *8*, 2789.
- [7] S.-I. Orimo, Y. Nakamori, J. R. Eliseo, A. Züttel, C. M. Jensen, *Chem. Rev.* **2007**, *107*, 4111.
- [8] P. Chen, M. Zhu, *Mater. Today* **2008**, *11*, 36.
- [9] E. Callini, Z. Ö. K. Atakli, B. C. Hauback, S.-I. Orimo, C. Jensen, M. Dornheim, D. Grant, Y. W. Cho, P. Chen, B. Hjörvarsson, P. Jongh, C. Weidenthaler, M. Baricco, M. Paskevicius, T. R. Jensen, M. E. Bowden, T. S. Autrey, A. Züttel, *Appl. Phys. A* **2016**, *122*, 1.
- [10] O. Zavorotynska, A. El-Kharbachi, S. Deledda, B. C. Hauback, *Int. J. Hydrogen Energy* **2016**, *41*, 14387.
- [11] H. W. Li, K. Kikuchi, Y. Nakamori, N. Ohba, K. Miwa, S. Towata, S. Orimo, *Acta Mater.* **2008**, *56*, 1342.
- [12] R. J. Newhouse, V. Stavila, S.-J. Hwang, L. E. Klebanoff, J. Z. Zhang, *J. Phys. Chem. C* **2010**, *114*, 5224.
- [13] N. Hanada, K. Chlopek, C. Frommen, W. Lohstroh, M. Fichtner, *J. Mater. Chem.* **2008**, *18*, 2611.
- [14] V. Ozolins, E. H. Majzoub, C. Wolverton, *Phys. Rev. Lett.* **2008**, *100*, 135501.
- [15] V. Ozolins, E. H. Majzoub, C. Wolverton, *J. Am. Chem. Soc.* **2009**, *131*, 230.
- [16] E. G. Bardají, N. Hanada, O. Zabara, M. Fichtner, *Int. J. Hydrogen Energy* **2011**, *36*, 12313.
- [17] A. Al-Kukhun, H. T. Hwang, A. Varma, *Int. J. Hydrogen Energy* **2012**, *37*, 17671.
- [18] G. Severa, E. Ronnebro, C. M. Jensen, *Chem. Commun.* **2010**, *46*, 421.
- [19] J. Zheng, X. Xiao, L. Zhang, S. Li, H. Ge, L. Chen, *J. Mater. Chem. A* **2017**, *5*, 9723.
- [20] A. Nale, F. Pendolino, A. Maddalena, P. Colombo, *Int. J. Hydrogen Energy* **2016**, *41*, 11225.
- [21] L. Zhang, J. Zheng, L. Chen, X. Xiao, T. Qin, Y. Jiang, S. Li, H. Ge, Q. Wang, *Int. J. Hydrogen Energy* **2015**, *40*, 14163.
- [22] O. Zavorotynska, I. Saldan, S. Hino, T. D. Humphries, S. Deledda, B. C. Hauback, *J. Mater. Chem. A* **2015**, *3*, 6592.
- [23] I. Saldan, C. Frommen, I. Llamas-Jansa, G. N. Kalantzopoulos, S. Hino, B. Arstad, R. H. Heyn, O. Zavorotynska, S. Deledda, M. H. Sørby, H. Fjellvåg, B. C. Hauback, *Int. J. Hydrogen Energy* **2015**, *40*, 12286.
- [24] I. Saldan, S. Hino, T. D. Humphries, O. Zavorotynska, M. Chong, C. M. Jensen, S. Deledda, B. C. Hauback, *J. Phys. Chem. C* **2014**, *118*, 23376.
- [25] Y. Pang, Y. Liu, M. Gao, L. Ouyang, J. Liu, H. Wang, M. Zhu, H. Pan, *Nat. Commun.* **2014**, *5*, 3519.
- [26] Y. Jia, C. Sun, S. Shen, J. Zou, S. S. Mao, X. Yao, *Renewable Sustainable Energy Rev.* **2015**, *44*, 289.
- [27] H. Shao, G. Xin, J. Zheng, X. Li, E. Akiba, *Nano Energy* **2012**, *1*, 590.
- [28] G. Xia, D. Li, X. Chen, Y. Tan, Z. Tang, Z. Guo, H. Liu, Z. Liu, X. Yu, *Adv. Mater.* **2013**, *25*, 6238.
- [29] P. E. de Jongh, P. Adelhelm, *ChemSusChem* **2010**, *3*, 1332.
- [30] M. Fichtner, *Phys. Chem. Chem. Phys.* **2011**, *13*, 21186.
- [31] T. K. Nielsen, F. Besenbacher, T. R. Jensen, *Nanoscale* **2011**, *3*, 2086.
- [32] X. Yu, Z. Tang, D. Sun, L. Ouyang, M. Zhu, *Prog. Mater. Sci.* **2017**, *88*, 1.
- [33] M. A. Wahab, D. J. Young, A. Karim, S. Fawzia, J. N. Beltramini, *Int. J. Hydrogen Energy* **2016**, *41*, 20573.
- [34] M. Han, Q. Zhao, Z. Zhu, Y. Hu, Z. Tao, J. Chen, *Nanoscale* **2015**, *7*, 18305.
- [35] Y. S. Au, Y. Yan, K. P. de Jong, A. Remhof, P. E. de Jongh, *J. Phys. Chem. C* **2014**, *118*, 20832.
- [36] Y. Yan, Y. S. Au, D. Rentsch, A. Remhof, P. E. de Jongh, A. Züttel, *J. Mater. Chem. A* **2013**, *1*, 11177.
- [37] F. Maximilian, Z.-K. Zhirong, H. Jianjiang, R. Arne, W. Peter, *Nanotechnology* **2009**, *20*, 204029.
- [38] M. A. Wahab, Y. Jia, D. Yang, H. Zhao, X. Yao, *J. Mater. Chem. A* **2013**, *1*, 3471.
- [39] G. Xia, Y. Tan, X. Chen, D. Sun, Z. Guo, H. Liu, L. Ouyang, M. Zhu, X. Yu, *Adv. Mater.* **2015**, *27*, 5981.
- [40] Y. Yan, A. Remhof, D. Rentsch, A. Züttel, *Chem. Commun.* **2015**, *51*, 700.
- [41] W. I. F. David, S. K. Callear, M. O. Jones, P. C. Aeberhard, S. D. Culligan, A. H. Pohl, S. R. Johnson, K. R. Ryan, J. E. Parker, P. P. Edwards, C. J. Nuttall, A. Amieiro-Fonseca, *Phys. Chem. Chem. Phys.* **2012**, *14*, 11800.
- [42] M. Chong, A. Karkamkar, T. Autrey, S.-I. Orimo, S. Jalisatgi, C. M. Jensen, *Chem. Commun.* **2011**, *47*, 1330.
- [43] Z. Lu, F. Ciucci, *Chem. Mater.* **2017**, *29*, 9308.
- [44] Y. Zhang, E. Majzoub, V. Ozoliņš, C. Wolverton, *Phys. Rev. B* **2010**, *82*, 174107.
- [45] M. Rueda, L. M. Sanz-Moral, A. Girella, P. Cofrancesco, C. Milanese, Á. Martín, *Int. J. Hydrogen Energy* **2016**, *41*, 15245.